numerically in fig. S1B. Note that at a tricritical point m_c, $t_{cm_c}(L \to \infty)$ is finite; for example, $t_{cm_c}(\infty) \approx 0.72$ in two dimensions, which is neither t_c nor unity, and the fluctuation is large and independent of N.

On the basis of the above results, we come to the conclusion that for $d < d_c = 6$, the percolation threshold in the limit $N \to \infty$ is t_c for $m < m_c$, finite t_{cm} at $m = m_c$, and 1 for $m > m_c$ [(*29*), equations 8 to 10]. For $d \geq d_c$, $m_c \to \infty$, and for finite m, $t_{cm} \to t_c$ (*29*). We conclude that when m is finite, the PT is continuous in the limit $N \to \infty$. In statistical physics, it is known that mean-field results above the upper critical dimension are equivalent to the solution on sparse random graphs. From this perspective, our result for $d > d_c$ is comparable to previous results for the EP model (*10*) on random graphs.

For the SCA model in the regime $m > m_c$ at $t_{cm}^{-}(L)$, we find that there are only a few clusters and that they are compact (Fig. 3A). Thus, the cluster size distribution at $t_{cm}^{-}(L)$ decays rapidly in the region of small cluster size and exhibits a peak in the region of large cluster size (Fig. 3B). The interface between clusters forms naturally along the bridge bonds and is self-affine. Because of the presence of already macroscopically grown but not yet spanning clusters, the order parameter is increased drastically when occupying a bridge bond. Finally, we note that for $d \geq d_c$, a discontinuous PT can take place if m varies with the system size N. We obtain a characteristic value $m_c \sim \ln N$ such that when m increases with N slower than m_c, the PT is continuous, and when m increases with N faster than m_c, the PT is discontinuous. They occur at t_c and 1, respectively [see (*29*)].

For the product rule (*4*), the nature of the PT is similar to the mean-field behavior of the SCA model in low dimensions such as $d = 2$. Under the best-of-m strategy, when m varies with the system size as $m > m_c \sim \ln N$, clusters are also compact and the number of clusters is limited to a finite value, and thus a discontinuous PT can take place. However, for a fixed m and in the thermodynamic limit, the PT is continuous [see (*29*)].

References and Notes

1. D. Stauffer, A. Aharony, *Introduction to Percolation Theory* (Taylor & Francis, London, ed. 2, 1994).
2. R. Pastor-Satorras, A. Vespignani, *Phys. Rev. Lett.* **86**, 3200 (2001).
3. M. Girvan, M. E. J. Newman, *Proc. Natl. Acad. Sci. U.S.A.* **99**, 7821 (2002).
4. D. Achlioptas, R. M. D'Souza, J. Spencer, *Science* **323**, 1453 (2009).
5. P. Erdös, A. Rényi, *Publ. Math. Inst. Hungar. Acad. Sci* **5**, 17 (1960).
6. R. M. Ziff, *Phys. Rev. Lett.* **103**, 045701 (2009).
7. Y. S. Cho, J. S. Kim, J. Park, B. Kahng, D. Kim, *Phys. Rev. Lett.* **103**, 135702 (2009).
8. F. Radicchi, S. Fortunato, *Phys. Rev. Lett.* **103**, 168701 (2009).
9. R. A. da Costa, S. N. Dorogovtsev, A. V. Goltsev, J. F. F. Mendes, *Phys. Rev. Lett.* **105**, 255701 (2010).
10. O. Riordan, L. Warnke, *Science* **333**, 322 (2011).
11. P. Grassberger, C. Christensen, G. Bizhani, S.-W. Son, M. Paczuski, *Phys. Rev. Lett.* **106**, 225701 (2011).
12. H. K. Lee, B. J. Kim, H. Park, *Phys. Rev. E* **84**, 020101(R) (2011).
13. N. Bastas, K. Kosmidis, P. Argyrakis, *Phys. Rev. E* **84**, 066112 (2011).
14. W. Choi, S.-H. Yook, Y. Kim, *Phys. Rev. E* **84**, 020102 (2011).
15. K. Panagiotou, R. Spöhel, A. Steger, H. Thomas, *Electron. Notes Discrete Math.* **38**, 699 (2011).
16. Y. S. Cho, B. Kahng, *Phys. Rev. Lett.* **107**, 275703 (2011).
17. W. Chen, R. M. D'Souza, *Phys. Rev. Lett.* **106**, 115701 (2011).
18. N. A. M. Araújo, H. J. Herrmann, *Phys. Rev. Lett.* **105**, 035701 (2010).
19. N. A. M. Araújo, J. S. Andrade Jr., R. M. Ziff, H. J. Herrmann, *Phys. Rev. Lett.* **106**, 095703 (2011).
20. K. J. Schrenk, N. A. M. Araújo, J. S. Andrade Jr., H. J. Herrmann, *Sci. Rep.* **2**, 348 (2012).
21. J. Nagler, A. Levina, M. Timme, *Nat. Phys.* **7**, 265 (2011).
22. H. D. Rozenfeld, L. K. Gallos, H. A. Makse, *Eur. Phys. J. B* **75**, 305 (2010).
23. J. Gómez-Gardeñes, S. Gómez, A. Arenas, Y. Moreno, *Phys. Rev. Lett.* **106**, 128701 (2011).
24. D. D. Martino, L. Dall'Asta, G. Bianconi, M. Marsili, *Phys. Rev. E* **79**, 015101(R) (2009).
25. R. K. Pan, M. Kivelä, J. Saramäki, K. Kaski, J. Kertész, *Phys. Rev. E* **83**, 046112 (2011).
26. Y. Azar, A. Z. Broder, A. R. Karlin, E. Upfal, *SIAM J. Comput.* **29**, 180 (1999).
27. M. Mitzenmacher, *IEEE Trans. Parallel Distrib. Syst.* **12**, 1094 (2001).
28. O. Riordan, L. Warnke, *Ann. Appl. Probab.* **22**, 1450 (2012).
29. See supplementary materials on *Science* Online.

Acknowledgments: We thank the referees for useful comments. Supported by National Research Foundation grant 2010-0015066 awarded through the Acceleration Research Program, the Seoul Science Foundation, and the Global Frontier Program (Y.S.C.).

Supplementary Materials

www.sciencemag.org/cgi/content/full/339/6124/1185/DC1
Supplementary Text
Figs. S1 to S11
Table S1

27 September 2012; accepted 28 January 2013
10.1126/science.1230813

Emergence of a Measurement Basis in Atom-Photon Scattering

Yinnon Glickman, Shlomi Kotler, Nitzan Akerman, Roee Ozeri*

After measurement, a wave-function is postulated to collapse on a predetermined set of states—the measurement basis. Using quantum process tomography, we show how a measurement basis emerges in the evolution of the electronic spin of a single trapped atomic ion after spontaneous photon scattering and detection. This basis is determined by the excitation laser polarization and the direction along which the photon was detected. Quantum tomography of the combined spin-photon state reveals that although photon scattering entangles all superpositions of the measurement-basis states with the scattered photon polarization, the measurement-basis states themselves remain classically correlated with it. Our findings shed light on the process of quantum measurement in atom-photon interactions.

The interaction between quantum systems and their environment results in decoherence and reduction of quantum superpositions to classical statistical ensembles. On the other hand, probing a fraction of the environment (environments by nature are too large to be monitored as a whole) yields information about the system state. The back-action on the system can then result in the emergence of a measurement basis. The measurement basis states will be those that are classically correlated with the detected environment modes, whereas their superpositions will be entangled with the environment (*1*, *2*). Thus, decoherence, measurement, and entanglement all partake in the quantum measurement process.

Because atomic systems can be well isolated from their environment and coherently controlled with good fidelity, they are a good experimental platform for the study of such fundamental quantum phenomena. In a typical experiment, a bipartite atomic superposition is controllably coupled to its environment and monitored in order to investigate different facets of decoherence and measurement. Examples include the study of decoherence due to coupling to engineered reservoirs by using trapped atomic ions (*3*) or the observation of the progressive decoherence of the measurement apparatus by using the interaction between atoms and a microwave cavity (*4*).

A natural environment for atomic systems is the electromagnetic vacuum to which they couple via spontaneous photon scattering. The effect of light scattering on the coherence of atomic interferometers showed that scattered photons expose the path an atom has taken (*5*–*7*). Photon scattering by trapped atomic ions, in which the direction and magnitude of the internal angular momentum of an atom become correlated with a scattered photon, results in spin decoherence (*8*–*10*). State-selective florescence by use of resonant laser light was used to measure the internal electronic state of atoms with a very small error probability (*11*–*13*). Last, the entanglement between a single atom and a spontaneously scattered photon was recently observed (*10*, *14*, *15*). In all of these experiments, decoherence, measurement, and entanglement

Department of Physics of Complex Systems, Weizmann Institute of Science, Rehovot 76100, Israel.

*To whom correspondence should be addressed. E-mail: roee.ozeri@weizmann.ac.il

were separately explored. However, the full dynamics of measurement of the atomic state by the electromagnetic vacuum environment was not observed. We show that a measurement basis emerges in the spin-state space of a single trapped atomic ion when photons are scattered and detected, in a process in which decoherence, measurement, and entanglement are intertwined.

We used the electronic spin, in the $5s^2S_{1/2}$ ground level, of a single trapped $^{88}Sr^+$ ion (Fig. 1). The ion was trapped and laser-cooled in a linear Paul trap. A weak magnetic field, applied in the $\hat{z}$ direction, removed the degeneracy between the two spin states by $\hbar\omega_0$, where $\omega_0/2\pi$ = 3.5 MHz, and $\hbar$ is Planck's constant h divided by 2π. Spin initialization, readout, and rotations were carried out by a combination of optical and radio frequency (rf) pulses (*13*, *16*, *17*). To ensure that the spin direction was well defined in the lab frame of reference, we reset the phase of our rf oscillator at the beginning of each repetition of the experiment. Subsequent to this initialization procedure, the spin performed Larmor precession around the $\hat{z}$ direction at ω_0.

Spin-photon interactions were induced by a 422-nm laser beam resonant with the $5s^2S_{1/2} \rightarrow 5s^2P_{1/2}$ transition (21 MHz spectral width) and polarized in the $\hat{z}$ direction (Fig. 1, inset). The ion scattered a photon from this beam with a probability between 0.05 and 0.1. Outgoing photons were detected from a direction perpendicular to the excitation laser direction ($\hat{x}$ direction). The outgoing photon polarization was fully characterized by a polarization analysis unit. The overall detection efficiency of scattered photons was measured to be roughly 1/400. We post-selected only those repetitions of the experiment in which a single photon was recorded. To investigate spin dynamics due to photon scattering, it is important to know the spin direction within the Larmor precession cycle at the moment the photon was scattered. To this end, we recorded the phase of our local oscillator—tuned to the Larmor precession frequency ω_0—at the time the scattered photon was recorded (*10*).

Photon scattering transfers the electron between two spin 1/2 manifolds ($5s^2S_{1/2} \rightarrow 5p^2P_{1/2}$). It is therefore convenient to think of the coupling between these manifolds in terms of spin 1/2 (Pauli) operators. In events in which a single photon was emitted into a direction $\hat{k}$, the spin degrees of freedom in the ground and excited states are coupled via a single application of the spin operator $i(\vec{\sigma} \cdot \vec{E})$ (*2*). Here, $\vec{\sigma}$ is a vector of the Pauli spin 1/2 operators, and $\vec{E}$ is the polarization vector of the emitted photon. In the case of absorption, the coupling operator is $-i\vec{\sigma} \cdot \vec{E}$ (*17*). It is instructive to study the reduced spin evolution, after photon emission, by using a circular photon polarization basis. In this case, the two spin operators that correspond to the emitted photon polarization components are $\vec{\sigma} \cdot \vec{E}_{\pm}{}^* = \sigma_{\pm}$, the spin ladder operators in the $\vec{k}$ direction. This means that spin states that initially point along the emitted photon propagation direction can emit circularly polarized photons but only with the helicity parallel to their spin. After emission of a circularly polarized photon, the spin direction reverses but remains aligned with the photon $\vec{k}$ vector. This is a simple manifestation of angular momentum conservation in the photon emission process. To evaluate spin evolution in the full scattering process, one has to account for photon absorption as well. Here, spin evolution depends on the polarization of the excitation laser and its

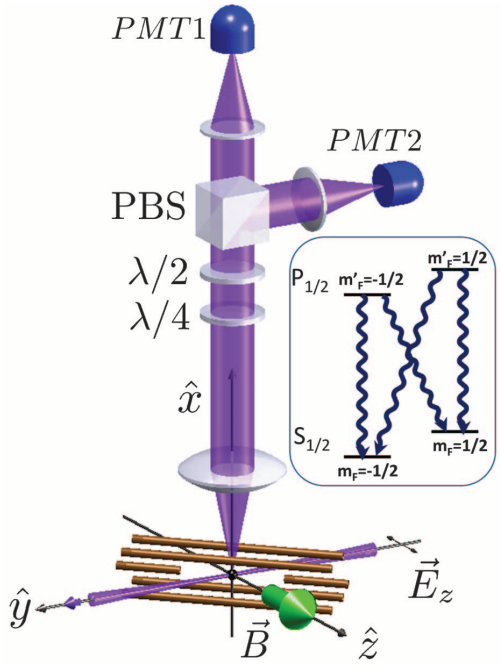

Fig. 1. Schematic of the experimental setup. A single $^{88}Sr^+$ ion is trapped in a linear Paul trap (*15*). The magnetic field is aligned along $\hat{z}$. (Inset) A schematic level structure of the $5s^2S_{1/2}$ and the $5p^2P_{1/2}$ electronic levels. The transition between these two levels is excited by a weak resonant beam, propagating along $\hat{y}$ and linearly polarized along $\hat{z}$. Scattered photons are collected along the $\hat{x}$ direction, and their polarization is analyzed by using half- and quarter-wave retardation plates and a PBS. The two ports of the PBS are directed toward two photo multiplier tube (PMT) detectors.

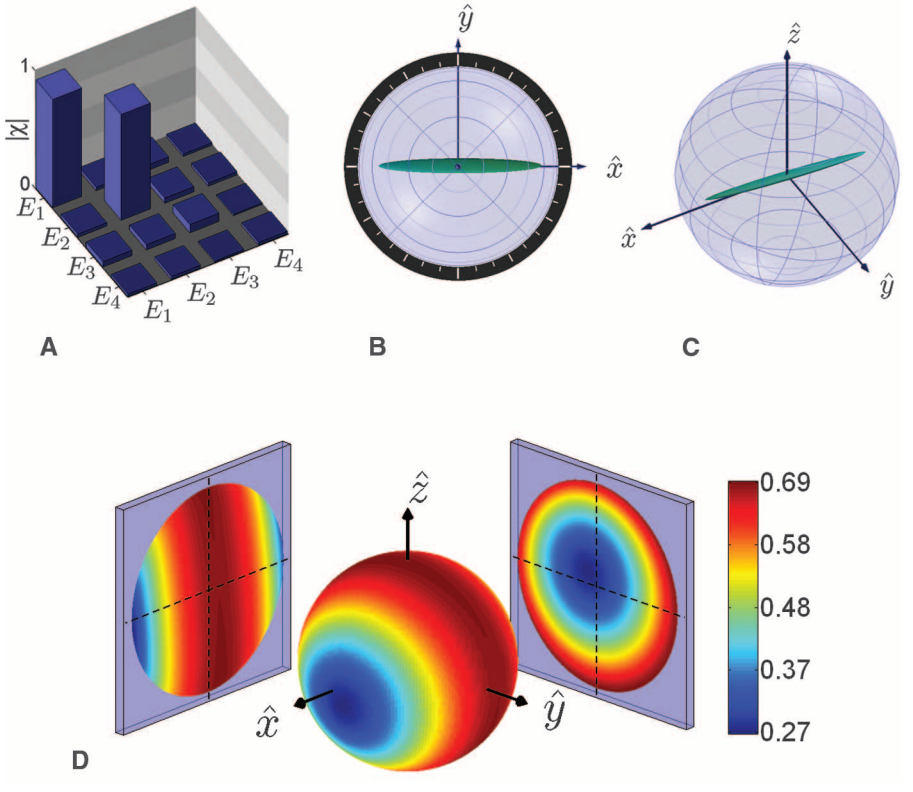

Fig. 2. Collapse of spin states. (**A**) The absolute value of the elements of the reconstructed process matrix, in the basis $E_1 = |\hat{x}\rangle\langle\hat{x}| = (I + \sigma_x)/2$, $E_2 = |-\hat{x}\rangle\langle-\hat{x}| = (I-\sigma_x)/2$ (projections on the $|\pm\hat{x}\rangle$ states), $E_3 = -i\sigma_y$, and $E_4 = \sigma_z$. (**B** and **C**) Two view points on the surface on which the Bloch sphere of initial spin states is mapped after photon detection. (**D**) The von Neumann entropy of post-scattering spin states plotted on the Bloch sphere of initial spin states.

direction relative to that of the scattered photon. In our experiment, the ion is excited with a laser beam that is linearly polarized in the $\vec{z}$ direction and photons are detected in the $\vec{x}$ direction (Fig. 1). The effect of a sequence of absorption and emission on the combined state of spin and emitted photons can then be expressed by an application of $\vec{\sigma}\cdot\vec{E}=\sigma_z$ followed by $S_{\mathrm{emit}}=\vec{\sigma}_{(+,x)}\otimes a^{\dagger}_{\vec{x},\vec{E}_+}+\vec{\sigma}_{(-,x)}\otimes a^{\dagger}_{\vec{x},\vec{E}_-}$, where $\vec{\sigma}_{(\pm,x)}=\sigma_y\mp i\sigma_z$ are the spin raising and lowering operators in the $\hat{x}$ direction. The spin-photon combined state after absorption and subsequent photon emission in the $\vec{x}$ direction hence evolves under

$$S_{\mathrm{scatt}}=\vec{\sigma}_{(+,x)}\vec{\sigma}_z\otimes a^{\dagger}_{\vec{x},\vec{E}_+}+\vec{\sigma}_{(-,x)}\vec{\sigma}_z\otimes a^{\dagger}_{\vec{x},\vec{E}_-}$$
$$=|-\hat{x}\rangle\langle-\hat{x}|\otimes a^{\dagger}_{\vec{x},\vec{E}_+}+|\hat{x}\rangle\langle\hat{x}|\otimes a^{\dagger}_{\vec{x},\vec{E}_-}\quad(1)$$

The spin of the ion is therefore projected along the emitted photon direction every time a photon with a circular polarization is detected. The pair of states $|\pm\hat{x}\rangle$ constitutes a measurement basis. These states are invariant under photon scattering (in the $\vec{x}$ direction), and therefore their entropy does not increase in the process. States that are initialized along this direction do not—whereas their superpositions do—entangle with the scattered photon polarization.

The correlation between the scattered photon and the basis along which spin states collapse can be well understood by angular momentum conservation arguments. Absorption of a $\hat{z}$-polarized photon flips $\hat{x}$-polarized spins (*18*). Circularly polarized emitted photons require full $\hbar$ angular momentum transfer along $\hat{x}$. The detection of circularly polarized photons therefore both measures and flips the spin in this direction. Spin states that are initially pointing in the $\hat{x}$ direction remain invariant under absorption followed by emission while the photon polarization measures the atomic spin along this direction. By post-selecting events in which the photon was scattered in a different direction, the basis along which the atomic spin is measured will change accordingly. Therefore, under continuous photon scattering from a linearly polarized beam, and without post-selection of a well-defined photon scattering direction, all resulting measurement directions will average to result in complete spin depolarization. An unpolarized excitation laser would have a similar effect.

We performed spin quantum process tomography (QPT) of post-selected events in which a single photon was detected. Typically, QPT is performed in a frame of reference that is rotating together with the spin. In this work, however, spin evolution due to photon scattering is determined by directions in the lab frame of reference. To faithfully perform QPT in the lab frame, we perform it stroboscopically with the spin Larmor precession. To this end, rather than analyzing all recorded events we limited our analysis to events that occurred within a $2\pi/32$-radian phase interval of our local oscillator. The direction of the spin at the moment of scattering, in these events, was spread over an angular span that equals this phase interval. Choosing other phase intervals of similar width yield identical results (*17*). We found that the process matrix is mostly composed of nearly equal contributions of projections on the $|+\hat{x}\rangle$ and $|-\hat{x}\rangle$ states, which is in agreement with Eq. 1. This is seen in Fig. 2A, in which the absolute value of the entries of the reconstructed process matrix is displayed. It is written by using the basis elements $|\hat{x}\rangle\langle\hat{x}|=(I+\sigma_x)/2$, $|-\hat{x}\rangle\langle-\hat{x}|=(I-\sigma_x)/2$ (projections on the $|\pm\hat{x}\rangle$ states), $-i\sigma_y$, and σ_z. The collapse of the spin wave function is best depicted in the Bloch sphere geometric representation. Each point on the surface of the Bloch sphere represents a pure state, whereas mixed states are represented as points within the sphere volume (*19*). After photon scattering, all prescattering pure states, represented by the Bloch sphere surface, are mapped onto a different surface, which is contained within the sphere. The reconstructed process matrix can be used to calculate the surface onto all pure spin state are mapped (Fig. 2, B and C). An elongated ellipsoid clearly marks the emergence of a spin measurement basis. We chose the direction along which the pointer basis emerges to be the $\hat{x}$ axis, thus coinciding this coordinate system with the lab coordinate system (Fig. 1). The 1:11 aspect ratio between the spheroid length along the emergent basis and its radial size is dictated by the finite local oscillator phase interval in our data, the finite numerical aperture of our photon collection lens, and quantum projection noise (*17*). The von Neumann entropy $S(\rho)=-\mathrm{Tr}[\rho\ln(\rho)]$ of all post-scattering states is shown in the color map in Fig. 2D. This is also the increase in entropy due to photon scattering. Spin states along the $\hat{x}$ direction indeed experience the minimal increase in entropy, which is in accordance with the predictability sieve criteria in decoherence theory (*1*). Other states, on the other hand, acquire entropy, demonstrating that without any knowledge of the scattered photon, the process of photon scattering is in general irreversible.

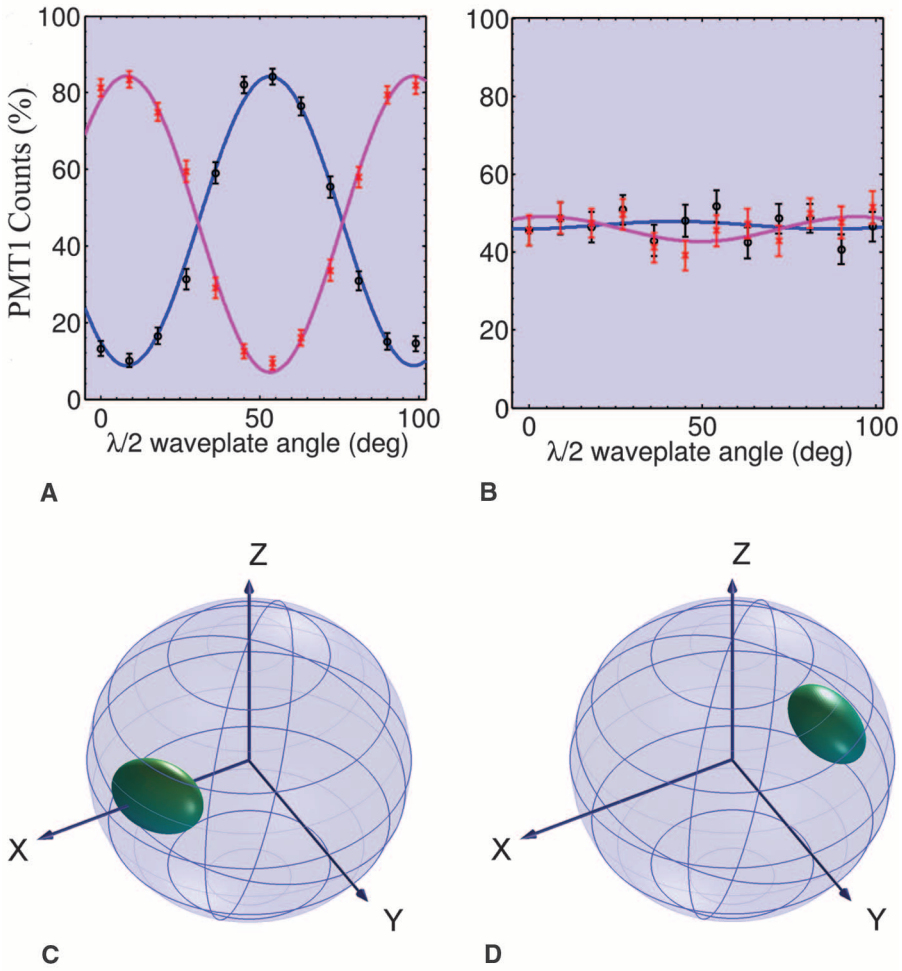

Fig. 3. Spin measurement via photon polarization detection. A quarter-wave retardation plate transformed the circular polarization of scattered photons into linear. The abscissa is the angle of the half-wave retardation plate, which is subsequently rotating the photon polarization direction with respect to that of the PBS. The ordinate is the probability of detecting photons on one port of the PBS when the spin is initialized to (**A**) the $|\hat{x}\rangle$ (solid red circles) or $|-\hat{x}\rangle$ (solid black circles) states or (**B**) the $|\pm Y\rangle$ states. (**C** and **D**) The surfaces representing all post-scattering states in which right or left circularly polarized photons were detected, respectively.

In order to prove that the $|\pm\hat{x}\rangle$ states on the poles of the emerging ellipsoid are a measurement basis, we analyzed the polarization of photons that were scattered by different initial spin states. According to Eq. 1, the $|\pm\hat{x}\rangle$ states scatter photons with a pure circular polarization, whereas other initial spin states become entangled with the photon polarization. The latter case leads to a statistical mixture of photon polarization measurement outcomes. The results of our photon polarization measurements are shown in Fig. 3. Here, we aligned a quarter-wave retardation plate so that it transformed the $|E_{\pm}\rangle$ states to an orthogonal linear basis. A proceeding half-wave plate rotated this linear polarization with respect to the basis of a polarization beam splitter (PBS). The probability of photon detection on a given port of the PBS versus the half-wave plate rotation angle is shown in Fig. 3A. Here, the spin is initialized to the $|\hat{x}\rangle$ (solid red circles) or $|-\hat{x}\rangle$ (solid black circles) states. As expected from a pure polarization state, this probability sinusoidally oscillates as the polarization is rotated. The blue and magenta solid lines are a sinusoidal fit to our data. Furthermore, whenever the two wave plates transform the emitted circular polarization to match the PBS basis, a clear correlation between the measured polarization and the initial spin state is observed. Similar data with the spin initialized to the $|\pm\hat{y}\rangle$ states is shown in Fig. 3B. As expected from a fully mixed polarization state, the photon detection probability on a given PBS port is independent of polarization rotation indicating a lack of classical correlation between the photon polarization state and the initial spin state. Alternatively, we performed spin QPT conditioned on the detection of right or left circularly polarized photons. The surfaces onto which all pure states are mapped are shown in Fig. 3, C (right-circular) and D (left-circular). Indeed, conditioned on the detection of a right circularly polarized photon, all initial states collapsed to the $|\hat{x}\rangle$ state, and conditioned on the detection of a left circularly polarized photon, all initial states collapsed to the $|-\hat{x}\rangle$ state.

Starting with an initial spin state other than $|\pm\hat{x}\rangle$, we have seen that both the spin state and the photon polarization state decohere into statistical mixtures. This decoherence is the result of spin-photon entanglement. To observe this entanglement, we preformed quantum state tomography of the combined spin-photon state. The reconstructed spin-photon density matrices for six different initial spin states are presented in Fig. 4, A to F: $|\pm\hat{z}\rangle$, $|\pm\hat{x}\rangle$, and $|\pm\hat{y}\rangle$. We plotted the density matrices using the $|\pm\hat{x}\rangle$ and $|E_{\pm}\rangle$ states as a basis. As seen, whenever the spin was initialized along $\pm\hat{x}$ the resulting spin-photon density matrices represent approximately separable states. Alternatively, spin states that were initially oriented along the $\pm\hat{y}$ or $\pm\hat{z}$ directions resulted in highly entangled states. We quantified the amount of atom-photon entanglement using the concurrence entanglement monotone, $C(\rho)$ (*20*). All atom-photon final density matrices were evaluated by means of linear combinations of the six reconstructed density matrices. A color map of the calculated concurrence values plotted on the Bloch sphere of initial spin states is presented in Fig. 4G. The minimum entanglement ($C < 0.03$) is along the $\hat{x}$ direction, whereas the maximally entangled states ($C \cong 0.7$) are along the sphere circumference in the $\hat{y}\hat{z}$ plane, which is consistent with the observed entropy increase shown in Fig. 2D.

We have shown that the back action of the observation of the atomic spin with light aligned it with our observation direction. States that were

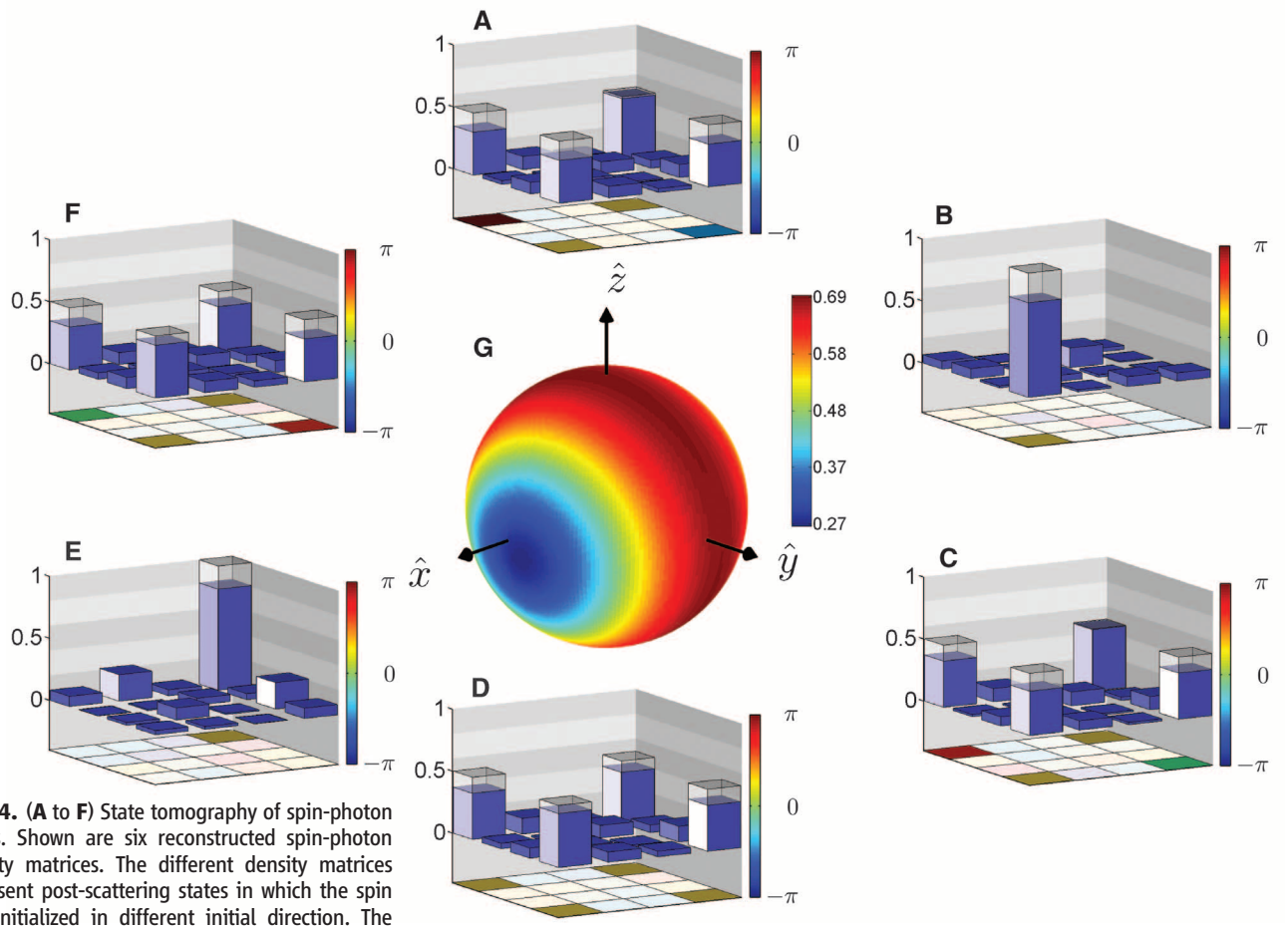

Fig. 4. (**A** to **F**) State tomography of spin-photon states. Shown are six reconstructed spin-photon density matrices. The different density matrices represent post-scattering states in which the spin was initialized in different initial direction. The different spin initial states are (A) $|\hat{z}\rangle$, (B) $|-\hat{x}\rangle$, (C) $|\hat{y}\rangle$, (D) $|-\hat{z}\rangle$, (E) $|\hat{x}\rangle$, and (F) $|-\hat{y}\rangle$. The density matrices are written in the basis of the product states $|\pm\hat{x}\rangle\otimes|E_{\pm}\rangle$. The solid bars are absolute values of entries of the reconstructed density matrices, whereas the transparent bars correspond to the values predicted with Eq. 1. The phases of the different entries are represented by different colors below the bars and according to the color map on the right. (**G**) A color map of the measured concurrence of every post-scattering spin-photon state. The map is plotted on the Bloch sphere of all initial pure spin directions.

initially aligned with this direction emitted pure circularly polarized photons and remained invariant under scattering. Their superpositions, on the other hand, became entangled with the scattered photon polarization. States that are invariant under coupling to the environment are of interest, not only because of their importance in the quantum measurement process but also because of their potential use for quantum control purposes. Invariant states can span decoherence-free subspaces in which quantum information can be protected (*21*). It would be therefore interesting to search for multi-spin states that are invariant under photon scattering, and detection, by using larger arrays of trapped ions.

References and Notes

1. W. H. Zurek, *Rev. Mod. Phys.* **75**, 715 (2003).
2. This mechanism is different than the process of ein-selection in decoherence theory, in which the mutual interaction between a quantum system, a measurement apparatus, and their environment results in the emergence of a preferred basis (*1*).
3. C. J. Myatt *et al.*, *Nature* **403**, 269 (2000).
4. M. Brune *et al.*, *Phys. Rev. Lett.* **77**, 4887 (1996).
5. M. S. Chapman *et al.*, *Phys. Rev. Lett.* **75**, 3783 (1995).
6. M. Mei, M. Weitz, *Phys. Rev. Lett.* **86**, 559 (2001).
7. D. A. Kokorowski, A. D. Cronin, T. D. Roberts, D. E. Pritchard, *Phys. Rev. Lett.* **86**, 2191 (2001).
8. R. Ozeri *et al.*, *Phys. Rev. Lett.* **95**, 030403 (2005).
9. H. Uys *et al.*, *Phys. Rev. Lett.* **105**, 200401 (2010).
10. N. Akerman, S. Kotler, Y. Glickman, R. Ozeri, *Phys. Rev. Lett.* **109**, 103601 (2012).
11. D. B. Hume, T. Rosenband, D. J. Wineland, *Phys. Rev. Lett.* **99**, 120502 (2007).
12. A. H. Myerson *et al.*, *Phys. Rev. Lett.* **100**, 200502 (2008).
13. A. Keselman, Y. Glickman, N. Akerman, S. Kotler, R. Ozeri, *New J. Phys.* **13**, 073027 (2011).
14. B. B. Blinov, D. L. Moehring, L. M. Duan, C. Monroe, *Nature* **428**, 153 (2004).
15. J. Volz *et al.*, *Phys. Rev. Lett.* **96**, 030404 (2006).
16. N. Akerman, S. Kotler, Y. Glickman, A. Keselman, R. Ozeri, *App. Phys. B*, 10.1007/s00340-011-4807-6 (2011).
17. Materials and methods are available as supplementary materials on *Science* Online.
18. Cohen-Tannoudji, Claude and Diu, Bernard and Laloe, Frank, *Quantum Mechanics* (Wiley-Interscience 2006), Vol. 2, p. 1048.
19. M. A. Nielsen, I. L. Chuang, *Quantum Computation and Quantum Information* (Cambridge Univ. Press, Cambridge, 2000).
20. M. B. Plenio, S. Virmani, *Quant. Inf. Comput.* **7**, 1 (2007).
21. D. A. Lidar, I. L. Chuang, K. B. Whaly, *Phys. Rev. Lett.* **81**, 2594 (1998).

Acknowledgments: Y.G. and S.K. have equally contributed to this work. We thank N. Davidsson and D. Stamper-Kurn for useful comments on the manuscript. We gratefully acknowledge the support by the Israeli Science Foundation, the Minerva Foundation, the German-Israeli Foundation for scientific research, the Crown Photonics Center, and M. Kushner Schnur, Mexico.

Supplementary Materials

www.sciencemag.org/cgi/content/full/339/6124/1187/DC1
Materials and Methods
Figs. S1 to S4

3 September 2012; accepted 2 January 2013
10.1126/science.1229650

A Transforming Metal Nanocomposite with Large Elastic Strain, Low Modulus, and High Strength

Shijie Hao,[1] Lishan Cui,[1]* Daqiang Jiang,[1] Xiaodong Han,[2]* Yang Ren,[3]* Jiang Jiang,[1] Yinong Liu,[4] Zhenyang Liu,[1] Shengcheng Mao,[2] Yandong Wang,[5] Yan Li,[6] Xiaobing Ren,[7,8] Xiangdong Ding,[7] Shan Wang,[1] Cun Yu,[1] Xiaobin Shi,[1] Minshu Du,[1] Feng Yang,[1] Yanjun Zheng,[1] Ze Zhang,[2,9] Xiaodong Li,[10] Dennis E. Brown,[11] Ju Li[7,12]*

Freestanding nanowires have ultrahigh elastic strain limits (4 to 7%) and yield strengths, but exploiting their intrinsic mechanical properties in bulk composites has proven to be difficult. We exploited the intrinsic mechanical properties of nanowires in a phase-transforming matrix based on the concept of elastic and transformation strain matching. By engineering the microstructure and residual stress to couple the true elasticity of Nb nanowires with the pseudoelasticity of a NiTi shape-memory alloy, we developed an in situ composite that possesses a large quasi-linear elastic strain of over 6%, a low Young's modulus of ~28 gigapascals, and a high yield strength of ~1.65 gigapascals. Our elastic strain-matching approach allows the exceptional mechanical properties of nanowires to be exploited in bulk materials.

It is challenging to develop bulk materials that exhibit a large elastic strain, a low Young's modulus, and a high strength because of the intrinsic trade-off relationships among these properties (*1*, *2*). A low Young's modulus in a single-phase material usually means weak interatomic bonding and thus low strength. Because of the initiation of dislocation activity and/or early failure caused by structural flaws, the elastic strain of bulk metals is usually limited to less than 1%. Because freestanding nanowires have ultrahigh elastic strain limits (4 to 7%) and yield strengths (*3*–*9*), it is expected that composites made with nanowires will have exceptional mechanical properties. However, the results obtained so far have been disappointing (*10*), primarily because the intrinsic mechanical properties of nanowires have not been successfully exploited in bulk composites (*10*–*12*). A typical example is the Nb nanowire–Cu matrix composite, in which the nanowires are well dispersed and well aligned, with strong interfacial bonding. The elastic strain limit achieved in the Nb nanowires in this type of composite is only ~1.5% (*13*, *14*), far below what may be expected of freestanding nanowires (*3*–*9*).

To optimize the retention of nanowire properties in a composite, we hypothesize that the matrix should not deform via sharp microscopic defects such as cracks or dislocations but rather should be rubbery or gluelike, which suggests the use of a shape-memory alloy (SMA) as the matrix. There are two main differences between an SMA matrix and a conventional, plastically deforming metal matrix. First, macroscopically, SMA supports a large pseudoelastic strain of ~7% by stress-induced martensitic transformation (SIMT) (*15*, *16*), which is a strain magnitude comparable to nanowire elasticity (*3*–*9*). Use of an SMA as the matrix allows one to match the high pseudoelasticity of the SMA with the high elasticity of nanowires, as illustrated in Fig. 1A. Second, SIMT and dislocation slip are fundamentally different processes at the atomic scale. Whereas the inelastic shear strain between two adjacent atomic planes approaches 100% after dislocation slip (*17*), the atomic-level inelastic or transformation strain is ~10% after SIMT in typical SMAs such as NiTi (*16*). Therefore, inelastic strain incompatibilities (which must be compensated for by the elastic strain field to maintain cohesion) are much milder at the SMA-nanowire interface than at typical dislocation–piled-up interfaces.

To verify this hypothesis, we selected Nb nanowires to be combined with a NiTi SMA. The NiTi-Nb system with ~20 atomic % Nb undergoes eutectic solidification into a microstructure consisting of fine Nb lamellae (*18*), which can be converted into Nb nanowires through severe plastic deformation. In this study, an ingot with a composition of $Ni_{41}Ti_{39}Nb_{20}$ (atomic %) was prepared by means of vacuum induction

[1]State Key Laboratory of Heavy Oil Processing, China University of Petroleum, Beijing 102249, China. [2]Institute of Microstructure and Properties of Advanced Materials, Beijing University of Technology, Beijing 100124, China. [3]X-ray Science Division, Argonne National Laboratory, Argonne, IL 60439, USA. [4]School of Mechanical and Chemical Engineering, The University of Western Australia, Crawley, WA 6009, Australia. [5]State Key Laboratory for Advanced Metals and Materials, University of Science and Technology Beijing, Beijing 100083, China. [6]School of Materials Science and Engineering, Beihang University, Beijing 100191, China. [7]State Key Laboratory for Mechanical Behavior of Materials and Frontier Institute of Science and Technology, Xi'an Jiaotong University, Xi'an 710049, China. [8]Ferroic Physics Group, National Institute for Materials Science, Tsukuba, 305-0047 Ibaraki, Japan. [9]State Key Laboratory of Silicon Materials, Zhejiang University, Hangzhou 310058, China. [10]Department of Mechanical Engineering, University of South Carolina, Columbia, SC 29208, USA. [11]Department of Physics, Northern Illinois University, De Kalb, IL 60115, USA. [12]Department of Nuclear Science and Engineering and Department of Materials Science and Engineering, Massachusetts Institute of Technology, Cambridge, MA 02139, USA.

*To whom correspondence should be addressed. E-mail: lishancui63@126.com (L.C.); xdhan@bjut.edu.cn (X.H.); ren@aps.anl.gov (Y.R.); liju@mit.edu (J.L.)